chemistry

MDPI

Article

Spin-Crossover 2-D Hofmann Frameworks Incorporating an Amide-Functionalized Ligand: *N*-(pyridin-4-yl)benzamide

Xandria Ong [1], Manan Ahmed [1], Luonan Xu [1], Ashley T. Brennan [1], Carol Hua [2], Katrina A. Zenere [3], Zixi Xie [3], Cameron J. Kepert [3], Benjamin J. Powell [4] and Suzanne M. Neville [1,*]

1 The School of Chemistry, The University of New South Wales, Sydney 2052, Australia; xandria.ong@unsw.edu.au (X.O.); manan.ahmed@unsw.edu.au (M.A.); luonan.xu@unsw.edu.au (L.X.); ashley.brennan@unsw.edu.au (A.T.B.)
2 School of Chemistry, The University of Melbourne, Parkville 3010, Australia; carol.hua@unimelb.edu.au
3 The School of Chemistry, The University of Sydney, Sydney 2006, Australia; katrina.zenere@sydney.edu.au (K.A.Z.); zixi.xie@sydney.edu.au (Z.X.); cameron.kepert@sydney.edu.au (C.J.K.)
4 School of Mathematics and Physics, The University of Queensland, St. Lucia 4072, Australia; powell@physics.uq.edu.au
* Correspondence: s.neville@unsw.edu.au

Abstract: Two analogous 2-D Hofmann-type frameworks, which incorporate the novel ligand *N*-(pyridin-4-yl)benzamide (benpy) $[Fe^{II}(benpy)_2M(CN)_4]\cdot 2H_2O$ (M = Pd (**Pd(benpy)**) and Pt (**Pt(benpy)**)) are reported. The benpy ligand was explored to facilitate spin-crossover (SCO) cooperativity via amide group hydrogen bonding. Structural analyses of the 2-D Hofmann frameworks revealed benpy-guest hydrogen bonding and benpy-benpy aromatic contacts. Both analogues exhibited single-step hysteretic spin-crossover (SCO) transitions, with the metal-cyanide linker (M = Pd or Pt) impacting the SCO spin-state transition temperature and hysteresis loop width (**Pd(benpy)**: $T_{\frac{1}{2}}\downarrow\uparrow$: 201, 218 K, ΔT: 17 K and **Pt(benpy)**: $T_{\frac{1}{2}}\downarrow\uparrow$: 206, 226 K, ΔT: 20 K). The parallel structural and SCO changes over the high-spin to low-spin transition were investigated using variable-temperature, single-crystal, and powder X-ray diffraction, Raman spectroscopy, and differential scanning calorimetry. These studies indicated that the ligand–guest interactions facilitated by the amide group acted to support the cooperative spin-state transitions displayed by these two Hofmann-type frameworks, providing further insight into cooperativity and structure–property relationships.

Keywords: spin crossover; Hofmann framework; hydrogen bonding

Citation: Ong, X.; Ahmed, M.; Xu, L.; Brennan, A.T.; Hua, C.; Zenere, K.A.; Xie, Z.; Kepert, C.J.; Powell, B.J.; Neville, S.M. Spin-Crossover 2-D Hofmann Frameworks Incorporating an Amide-Functionalized Ligand: *N*-(pyridin-4-yl)benzamide. *Chemistry* **2021**, *3*, 360–372. https://doi.org/10.3390/chemistry3010026

Received: 14 December 2020
Accepted: 20 February 2021
Published: 1 March 2021

1. Introduction

SCO can occur in d^4 to d^7 transition metals, whereby a reversible transition between low-spin (LS) and high-spin (HS) states occurs with the application of external stimuli (e.g., magnetic field, light irradiation, temperature, pressure) [1–6]. Of these, Fe^{II} complexes are the most widely reported as they exhibit versatile SCO behaviors, including abrupt and hysteretic transitions and multi-stepped pathways [7–10]. Solid-state cooperativity, defined as the effectiveness of the propagation of SCO effects throughout the material, arises in Fe^{II} complexes as there is a strong coupling of spin-state switching to the lattice due the large volume change between HS and LS states (5–12%). [10–13] As cooperativity is dependent on the strength of communication between metal centers, the direct bridging of switching metal ions in extended networks (i.e., coordination polymers (CPs) and metal-organic frameworks (MOFs)) is an effective approach [9,14–22], as well as via supramolecular interactions, such as hydrogen bonds and aromatic contacts [10]. One of the most intensively explored SCO CP families is Hofmann frameworks, which are typically characterized by Fe^{II} sites bridged by square planar $[M(CN)_4]^{2-}$ groups (M = Pd, Pt, or Ni) and connected (3-D) or spaced (2-D) into frameworks by *N*-donor aromatic organic ligands [9,14–22].

Effective SCO communication in these materials comes from the metallocyanide groups and can be modulated by the organic ligand and encapsulated guest molecules. Hence, the choice of organic ligand incorporated into Hofmann frameworks has a significant effect on the SCO properties observed, and, thus, substantial focus has been directed at structure-function studies with various ligand functional groups and lengths. For example, in the 2-D Hofmann framework $[Fe^{II}(pyridine)_2M(CN)_4]$ (M = Pd or Pt) a thermally induced, single-step hysteretic SCO transition was observed ($T_{\frac{1}{2}}\downarrow\uparrow$: 208, 213 K; ΔT = 5 and $T_{\frac{1}{2}}\downarrow\uparrow$: 208, 216 K; ΔT = 8, for the Pd and Pt analogues, respectively) [15]. When pyrazine was used in place of pyridine to form the 3-D Hofmann analogue $[Fe^{II}(pyrazine)Pd(CN)_4]$, a higher transition temperature and a wider hysteresis loop ($T_{\frac{1}{2}}\downarrow\uparrow$: 220, 240 K; ΔT = 20 K) was observed [15]. However, framework dimensionality alone is not the only possible influencing factor on SCO cooperativity. For example, pyridine functionalization in the 2-D framework $[Fe^{II}(4\text{-phenylpyridine})_2Pd(CN)_4]$ resulted in an increased transition temperature compared to the pyridine analogue and an impressive hysteresis loop width of 40 K [23]. Structural studies on this analogue highlight that, alongside the framework connectivity, aromatic contacts play a large role in enhancing the SCO communication. Likewise, the use of the ligand 3-aminopyridine in the 2-D Hofmann framework $[Fe(3\text{-aminopyridine})_2M(CN)_4]$ (M = Ni, Pd or Pt) emphasizes the significance of hydrogen bonds on cooperativity enhancement. High transition temperatures and wide (>20 K) thermal hysteresis loops were observed for both the Pt and Pd analogues (Pd: $T_{\frac{1}{2}}\downarrow\uparrow$: 169, 206 K; ΔT = 37 K and Pt: $T_{\frac{1}{2}}\downarrow\uparrow$: 183, 213 K; ΔT = 30) [24]. Hence, the concept of targeting increased SCO cooperativity by both incorporating SCO sites into CPs and also including functionalized ligands with hydrogen bonding and/or aromatic interaction capacity serves as the basis for the materials prepared in this report. We utilized the ligand *N*-(pyridin-4-yl)benzamide (benpy; Figure 1) [25] to facilitate SCO cooperativity via both hydrogen bonding from the amide functional group and aromatic contacts via the aromatic rings (Figure 1). Amide-functionalized ligands were successfully applied to a range of SCO framework previously, resulting in a range of interesting structures and SCO features [26–30] based on interaction with the amide group. Here, we report the structure and SCO properties of the 2-D Hofmann frameworks' analogues $[Fe^{II}(benpy)_2(M(CN)_4)]$ (M = Pd and Pt) with an interest in the impact of amide group contacts on the structure and cooperativity of the spin-state transition.

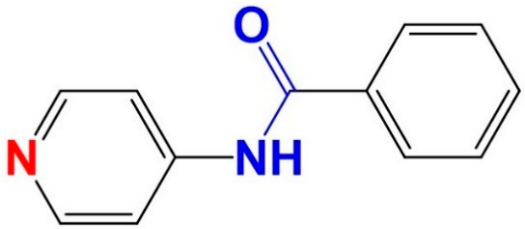

Figure 1. *N*-(pyridin-4-yl)benzamide (benpy) with metal coordination site (red), potential hydrogen bonding (blue), and aromatic (black) interaction sites indicated.

2. Materials and Methods

Reagents were purchased commercially from Sigma-Aldrich or Merck and not further purified before use. Care was taken, handling $Fe(ClO_4)_2 \cdot 6H_2O$ only in small amounts to avoid any potential explosions.

2.1. Synthesis of N-(pyridin-4-yl)benzamide (benpy)

The 4-aminopyridine (1.69 g, 18.0 mmol) and triethylamine (2.28 g, 22.5 mmol) were dissolved in CH_2Cl_2 (30 mL). This solution was placed in an ice bath, wherein benzoyl chloride (2.11 g, 15.0 mmol) was added with continuous stirring once the temperature reached 0 °C. The mixture was then allowed to return to room temperature while stirring for 1 h. The translucent, needle-like precipitate was collected via filtration and washed with excess CH_2Cl_2. The crude product was recrystallized using 1:1 EtOH:H2O (1.63 g,

8.22 mmol, 54.8%). The ^{1}H NMR (d_6-DMSO, 300 MHz): δ = 7.53–7.66 (m, J_{HH} = 15.22 Hz, 3H), 7.78 (d, J_{HH} = 1.46 Hz, 2H), 7.96 (d, J^{HH} = 6.90 Hz, 2H), 8.47 (d, J_{HH} = 6.27 Hz, 2H), and 10.59 (s, 1H). The ^{13}C NMR (d_6-DMSO, 75 MHz): δ = 114.0, 127.9, 128.6, 132.1, 145.9, 150.5, and 166.5. ESI-MS (ESI$^+$, m/z) calculated $[M + H]^+$ for $C_{12}H_{10}N_2O$: 198.08 found 199.08. IR (solid, ν/cm^{-1}): 3241.3 (w), 3158.6 (w), 1673.5 (vs), 1586.3 (vs), 1503.1 (vs), 1414.7 (m), 1327.4 (s), 1292.0 (s), 1262.4 (w), 1207.5 (s), 1109.8 (w), 1090.8 (w), 1074.4 (w), 1027.4 (m), 991.1 (m), 932.4 (w), 892.9 (m), 822.6 (vs). Elemental analysis (%) calculated C 72.71, H 5.09, N 14.13 and found C 72.02, H 4.64, N 14.03.

2.2. Synthesis of $[Fe^{II}(benpy)_2Pd(CN)_4]\cdot 2H_2O$ (Pd(benpy))

Vial-in-vial slow diffusion methods were used to prepare a bulk crystalline sample. Solid $Fe(ClO_4)_2\cdot 6H_2O$ (15.0 mg, 0.059 mmol) was weighed into a small vial and $K_2Pd(CN)_4$ (17.0 mg, 0.059 mmol) and benpy (23.4 mg, 0.118 mmol) were weighed into a larger vial. The small vial was placed within the larger vial before 1:1 EtOH:H_2O (~20 mL) solvent was added slowly to fill both vials to the top. Yellow crystals with square-plate morphology formed over six weeks. IR (solid, ν/cm^{-1}): 3533.4 (m), 2170.8 (s), 1594.5 (vs), 1523.2 (s), 1422.3 (s), 1337.8 (s), 1299.5 (s), 1263.1 (m), 1210.8 (s), 1097.0 (w), 1069.3 (w), 1015.7 (m), 997.7 (w), 929.9 (w), 892.8 (w), 830.4 (s), 707.1 (vs), 682.8 (s). Elemental analysis (air-dried sample) calculated (%) C 50.74 H 3.04 N 16.91 and found (%) C 50.57 H 3.28 N 17.01.

2.3. Synthesis of $[Fe^{II}(benpy)_2Pt(CN)_4]\cdot 2H_2O$ (Pt(benpy))

Vial-in-vial slow diffusion methods were used to prepare a bulk crystalline sample. Solid $Fe(ClO_4)_2\cdot 6H_2O$ (15.0 mg, 0.059 mmol) was weighed into a small vial and $K_2Pt(CN)_4$ (22.3 mg, 0.059 mmol) and benpy (23.4 mg, 0.118 mmol) were weighed into a larger vial. The small vial was placed within the larger vial before 1:1 EtOH:H2O (~20 mL) solvent was added slowly to fill both vials to the top. Yellow crystals with square-plate morphology formed over six weeks (100% yield). IR (solid, ν/cm^{-1}): 3544.0 (b), 2168.0 (s), 1594.4 (br), 1524.0 (br), 1422.1 (m), 1337.6 (m), 1299.3 (m), 1262.3 (w), 1210.8 (m), 1096.3 (w), 1069.1 (aw), 1015.5 (w), 967.9 (w), 928.5 (w), 892.3 (w), 830.4 (s), 732.9 (w), 706.5 (s), 666.2 (w). Elemental analysis (air-dried sample) calculated (%) C 44.71 H 2.88 N 14.56 and found (%) C 43.97 H 2.98 N 14.75.

2.4. Thermogravimetric Analysis (TGA)

Crystalline samples were loaded onto a platinum pan and measured on a TA Instruments Discovery TGA Analyzer at a ramp rate of 1 °C min^{-1} (RT–500 °C) under a dry N_2 gas environment (20 mL min^{-1}).

2.5. Variable-Temperature, Single-Crystal X-ray Diffraction Analysis (VT-SCXRD)

Data were collected at the Australian Synchrotron macromolecular crystallography (MX1) beamline radiation source [31]. Data were collected using a Dectris Eiger 9M detector and Si<111> monochromated synchrotron radiation (λ = 0.71073 Å). The data were collected using the BlueIce software [32] and were processed using the XDS software [33]. All structures were solved using SHELXT [34] and refined using SHELXL [35] within the OLEX2 graphical user interface [36]. Hydrogen atoms were placed at idealized positions and refined using the riding model. Details of the crystallographic data collection and refinement parameters are summarized in Table 1 and selected parameters are presented in Table S2. The data have been deposited in the Cambridge Crystallographic Data Centre (CCDC) and are freely available at CCDC: 2049372-2049375.

Table 1. Representative structural details for **Pd(benpy)** and **Pt(benpy)** in the LS and HS states.

	$Fe^{II}(benpy)_2Pd(CN)_4 \cdot 2H_2O$		$Fe^{II}(benpy)_2Pt(CN)_4 \cdot 2H_2O$	
Spin state	LS	HS	LS	HS
Temperature (K)	100	250	100	250
Average Fe–N≡C	1.9976	2.1411	1.926	2.125
Average Fe–N(py)	1.93775	2.2042	1.997	2.216
Average Fe–N (Å)	1.9577	2.1621	1.950	2.155
O·water (Å)	2.767(2)	2.846(2)	2.730(2)	2.805(2)
water·N(H) (Å)	2.852(4)	2.904(2)	2.895(2)	2.915(3)
Σ (Fe) (°)	13.20	8.160	12.82	12.40
Ligand torsion (°)	24.3	35.5	13.8	40.3

2.6. Variable-Temperature, Powder X-ray Diffraction Analysis (VT-PXRD)

Data were collected at the Powder Diffraction beamline BL-10 (20.0 keV, 0.589062 Å) at the Australian Synchrotron [37]. A polycrystalline sample was loaded into 0.7-mm-diameter borosilicate glass capillary and mounted onto the powder diffraction beamline. The capillaries were rotated at ~1 Hz during data collection to assist in powder averaging. The beamline was set up with a nominal wavelength of 1.0 Å; the wavelength was determined accurately using NIST SRM660b LaB_6 standard. Temperature-dependent data were then collected continuously over the range 175–250 K. Data were collected using a Mythen microstrip detector [38] from 1.5° to 75° in 2θ. To cover the gaps between detector modules, two data sets, each of 60 s in duration, were collected with the detector set 5° apart and they were then merged to give a single data set using PDViper [39]. A slit size of 2 mm was used to ensure that the fraction of the capillary illuminated by the X-ray beam was the same as the isothermal zone on the cryostream. Le Bail analysis and peak fitting were performed using the TOPAS software package [40].

2.7. Variable-Temperature Magnetic Susceptibility

Variable-temperature magnetic susceptibility data were obtained using a Quantum Design VersaLab magnetometer with a Vibrating Sample Magnetometer (VSM) accessory attached. Measurements were taken continuously over the range 150–300 K under a 0.3 T magnetic field with sweep rates of 0.5, 1, 2, and 4 K min^{-1}. The crystalline samples were loaded into polypropylene holders (Formolene 4100 N) and clipped into a brass half-tube for analysis.

2.8. Differential Scanning Calorimetry (DSC)

Measurements were taken at 10 K min^{-1} (294–190 K) using a Netzsch DSC 204 F1 Phoenix with a liquid nitrogen cooling cryostat. The crystals were placed into a 40-µL aluminum crucible and sealed. Instrument calibrations were made using sapphire standards with the sample holder kept dry and under a constant, dry N_2 flow (20 mL min^{-1}). The Netzsch Proteus Analysis 2019 software was used to process the data.

2.9. Calculation of the Magnetic Susceptibility

The magnetic susceptibility was calculated from the Slichter–Drickamer model [41,42], which predicts that the HS fraction, γ_{HS}, is given by

$$\gamma_{HS}(T) = \frac{1}{1 + \exp\left[\frac{\Delta H + \Gamma(1-2\gamma_{HS}(T))}{RT} - \frac{\Delta S}{R}\right]}, \quad (1)$$

where ΔH and ΔS are, respectively, the enthalpy and entropy differences between the HS and LS states, R is the gas constant, and Γ parameterizes the interactions between metal

centers. We neglected magnetic interactions between metals in the HS state, whence one finds that the magnetic susceptibility is given by

$$\chi(T) = [1 - \gamma_{HS}(T)]\chi_{LS} + \gamma_{HS}\chi_{HS}, \quad (2)$$

where χ_{LS} (χ_{HS}) is the susceptibility in the LS (HS) state. For both **Pd(benpy)** and **Pd(benpy)** we obtained the best fits on constraining $\chi_{LS} = 0$ and $\chi_{HS}T = 3.6$ cm^3 K mol^{-1}. No closed form solution was known for the transcendental Equation (1), so a numerical solution was obtained self-consistently for a range of parameters (ΔH, ΔS, and Γ), with the best fit taken as the parameters with the lowest root-mean-square error relative to the measured susceptibility. We swept through parameters three times, each time narrowing the range but moving through finer steps, to obtain accurate solutions in a reasonable time.

The Slichter–Drickamer model is equivalent to a mean field treatment of the Ising–Wajnflasz–Pick model [42,43]. Like all mean field theories, it is more accurate in higher dimensions. So long as the interlayer elastic interactions are not too small (compared to k_BT), **Pd(benpy)** and **Pd(benpy)** are three-dimensional materials and mean field theory should be reasonable. The anisotropy between the intra- and interlayer elastic interactions is only captured on average but does not affect the applicability of the theory. If the interlayer elastic interactions are small compared to k_BT, then **Pd(benpy)** and **Pd(benpy)** are two-dimensional materials. As we did not discuss critical behavior below a mean field, approximation is reasonable in either case.

2.10. Variable-Temperature Raman Spectroscopy

Raman spectra were collected on a Renishaw inVia-Qontor upright microscope. The excitation wavelength of 785 nm (20 mW at 10% laser power, L ×50 objective) was used to acquire the Raman spectra in the range 150–2300 cm^{-1} with a 10-s exposure time. The samples were loaded into 0.7-mm-diameter glass capillaries and mounted on a Linkam-FTIR 600 variable temperature stage. Liquid nitrogen was continuously flowed onto the Linkam stage with a temperature programmer and cooling pump connected. Data were collected over the range 170–250 K at 10-K steps.

3. Results and Discussion

3.1. Synthesis and Characterization

The two materials **Pd(benpy)** and **Pt(benpy)** were successfully synthesized as bulk crystalline solids via slow diffusion methods. Their purity was confirmed via elemental analysis (CHN), IR spectroscopy, Le Bail analysis of the PXRD data (Figures S4 and S5) and TGA measurements. The TGA data (Figure S1) showed an initial mass loss below ~50 °C (**Pd(benpy)**: 4.90% and **Pt(benpy)**: 4.33%) corresponding to a theoretical loss of two solvent water molecules per Fe^{II} site (calculated for **Pd(benpy)**: 4.58% and **Pt(benpy)**: 4.07%). There was no further mass loss until ~300 °C, when framework decomposition occurred.

3.2. Spin-Crossover Properties

3.2.1. Variable-Temperature Magnetic Susceptibility

A color change from yellow to red was observed when the crystals of **Pd(benpy)** and **Pt(benpy)** were cooled with liquid N_2, indicative of a HS to LS transition (Figure S2). Variable-temperature magnetic susceptibility measurements (300–150 K) revealed hysteretic, single-step SCO transitions (Figure 2a,b). The $\chi_M T$ values remained constant at ~3.50 cm^3 Kmol^{-1} from 300 to 196 K for **Pd(benpy)** and 300–203 K for **Pt(benpy)**, corresponding to HS Fe^{II} sites (S = 2) [10]. Below this, a rapid decrease in $\chi_M T$ values occurred, to ~0.1 cm^{3}Kmol^{-1}, indicative of a complete HS to LS (S = 0) transition of the Fe^{II} sites. The scan rate dependence of the SCO transition was explored (rates: 0.5, 1, 2, and 4 K min^{-1}; Figure 2a,b. Extrapolation of the scan rate versus transition temperature (Figure S3) revealed zero-scan rate transition temperatures of $T_{\frac{1}{2}}\downarrow\uparrow$: 201, 218 K ($\Delta T$: 17 K) for **Pd(benpy)** and $T_{\frac{1}{2}}\downarrow\uparrow$: 206, 226 K ($\Delta T$: 20 K) for **Pt(benpy)**. The higher transition

temperature observed in the Pt analogue compared to the Pd analogue was consistent with other Hofmann-type frameworks [9,14–22]. The abrupt transition character and approximate transition temperatures and hysteresis loop width were consistent with other 2-D Hofmann frameworks [44].

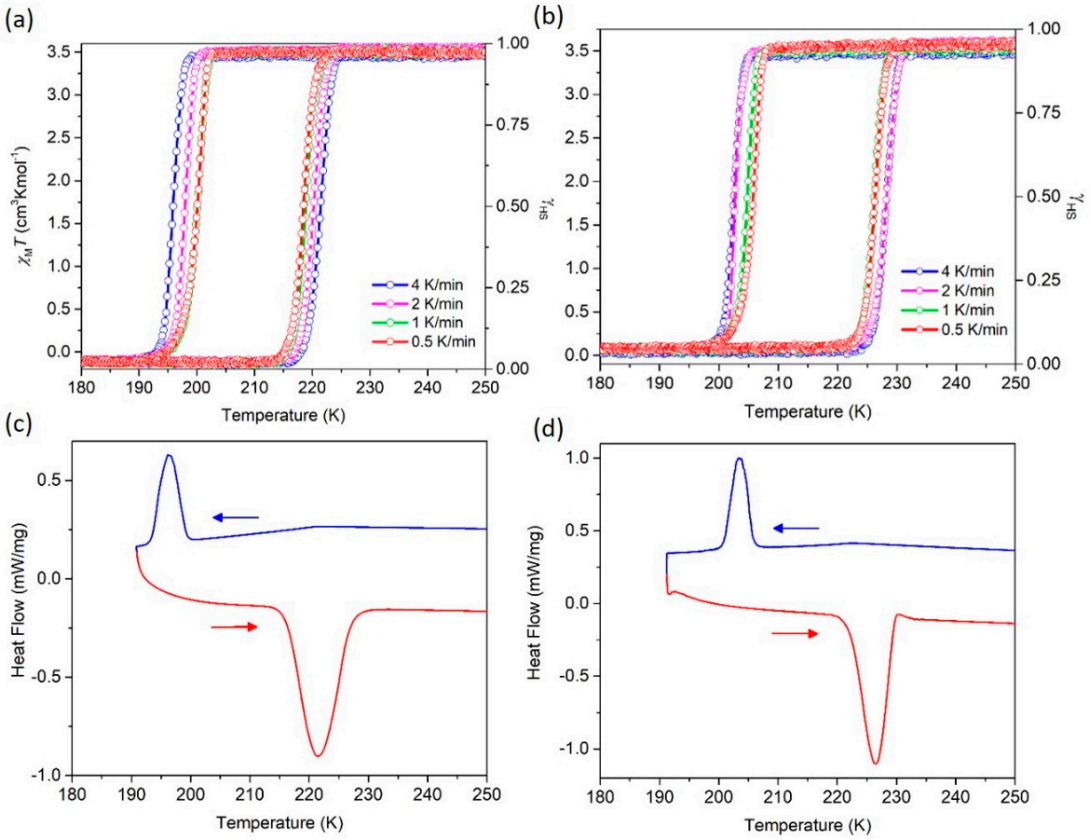

Figure 2. $\chi_M T$ (and HS fraction) versus temperature for (**a**) **Pd(benpy)** and (**b**) **Pt(benpy)**, variable scan rate data are shown. Differential scanning calorimetry data for (**c**) **Pd(benpy)** and (**d**) **Pt(benpy)**.

3.2.2. Differential Scanning Calorimetry

DSC measurements (Figure 2c,d) show an endothermic peak on cooling and an exothermic peak on heating for both **Pd(benpy)** and **Pt(benpy)**. The peak maxima, **Pd(benpy):** 196, 222 K and **Pt(benpy)**: 204, 226 K, were consistent with the $T_{\frac{1}{2}}$ values recorded by magnetic susceptibility (The DSC data were collected at 10 Kmin$^{-1,}$ thus a slight difference was anticipated compared to the magnetic susceptibility data). The thermodynamic parameters from these data were **Pd(benpy)**: ΔH_{avg} = 15.7 ± 2 kJ mol^{-1}, ΔS_{avg} = 75.3 ± 5 J K^{-1} mol^{-1} and **Pt(benpy)**: ΔH_{avg} = 17.9 ± 2 kJ mol^{-1} and ΔS_{avg} = 83.3 ± 4 J K^{-1} mol^{-1}, obtained from an average of the cooling and heating peaks. Enthalpy and entropy values of 10–20 kJ mol^{-1} and 35–90 J K^{-1} mol^{-1} values are typical for Fe^{II} SCO [45], in particular, Hofmann frameworks [9,14–22].

3.2.3. Magnetic Susceptibility Calculation

The spin transition curves were calculated from the Slichter–Drickamer model (Figures S4 and S5) [41,42]. The parameters extracted from the fits for **Pd(benpy)** were ΔH = 14.5 kJ mol^{-1}, ΔS = 68.9 J K^{-1} mol^{-1}, and Γ = 5.38 kJ K^{-1} mol^{-1} and for **Pt(benpy)** were ΔH = 20.8 kJ mol^{-1}, ΔS = 96.1 J K^{-1} mol^{-1}, and Γ = 5.90 kJ mol^{-1}. The ΔH and ΔS values agreed well with the DSC data.

There were three contributions to the entropy difference between the HS and LS states, $\Delta S = \Delta S_{spin} + \Delta S_{orb} + \Delta S_{vib}$. For Fe^{II} the spin contribution was $\Delta S_{spin} = R \ln 5 \simeq 13.4$ J K^{-1} mol^{-1} and the orbital contribution was $\Delta S_{orb} = R \ln 3 \simeq 9.1$ J K^{-1} mol^{-1}, thus the vibrational

contribution was $\Delta S_{vib} = 46.4$ J K^{-1} mol^{-1} for **Pd(benpy)** and $\Delta S_{vib} = 73.6$ J K^{-1} mol^{-1} **Pt(benpy)**, based on the fits to the Slichter–Drickamer model. (Using the calorimetry values of ΔS yielded $\Delta S_{vib} = 52.8$ J K^{-1} mol^{-1} for **Pd(benpy)** and $\Delta S_{vib} = 60.8$ J K^{-1} mol^{-1} **Pt(benpy)**).

It can be shown [43] that the Slichter–Drickamer model is equivalent to the mean-field solution of the long-range Ising–Wajnflasz–Pick model and, thence, that

$$\Gamma = 2 \sum_{n,m} J_{n,m}, \quad (3)$$

where $J_{n,m}$ is the coupling between metal centers n unit cells apart in the crystallographic a-direction and m unit cells apart in the crystallographic b-direction. Thus, Γ measures the sum of the microscopic interactions, $J_{n,m}$, which, in turn, can be related to the underlying elastic interactions in the material [43]. Thus, the large positive values of Γ (37% of ΔH in **Pd(benpy)** and 28% of ΔH in **Pt(benpy)**) showed that the sum of the elastic interactions in both materials was significant and ferroelastic. Overall, the modeling showed that the spin-state transitions in both **Pd(benpy)** and **Pt(benpy)** were strongly cooperative.

3.3. Variable-Temperature Structural Analysis

3.3.1. Variable-Temperature Powder X-ray Diffraction

Data were collected to monitor the structure variation over the SCO transition (250–175 K). Figure 3a and Figure S8a show the evolution of a selected Bragg peak (2θ = 6.5–6.8°, *hkl*: 011) for **Pd(benpy)** and **Pt(benpy)**, respectively, over the HS to LS to HS transition. These data are also presented as peak position versus temperature (Figures S8b and S9), showing SCO character and transition temperatures consistent with magnetic susceptibility data. All of the data over the temperature range 250–175–250 K were fitted by Le Bail refinement. These data: (1) confirmed the bulk purity of the samples (Figures S6 and S7), (2) confirmed the symmetry and space group, and (3) allowed the temperature dependence of the unit cell parameters to be assessed. Figure 3b and Figure S11d show the unit cell volume evolution for **Pd(benpy)** and **Pt(benpy)**, respectively, confirming the abrupt single-step volumetric change over the reversible spin-state transition and an overall volume change of ~5.5%, consistent with a complete HS to LS transition. The evolution of the unit cell lengths for **Pd(benpy)** and **Pt(benpy)** are shown in Figures S10 and S11, respectively. The transition temperatures from VT-PXRD data were ca. 5 K lower than that observed by magnetic susceptibility. This is not uncommon due to the differences in experimental conditions. Here, the ramp rate for data collection was much faster for VT-PXRD than magnetic susceptibility.

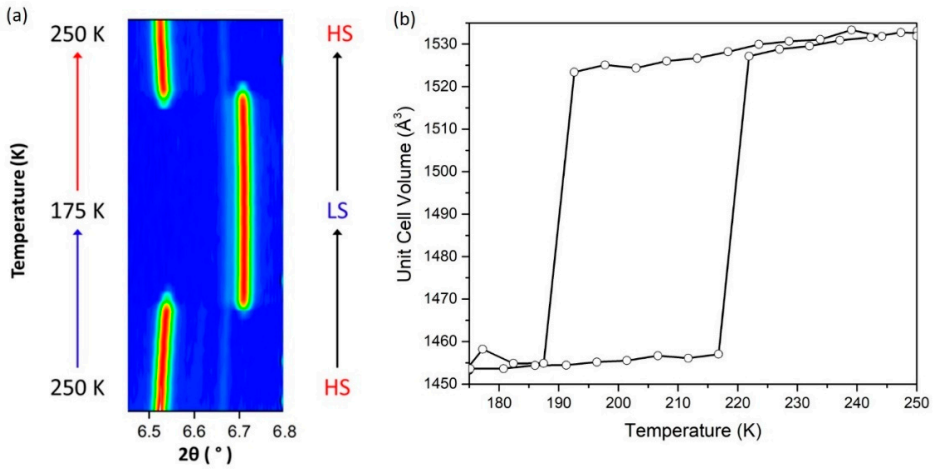

Figure 3. VT-PXRD data for **Pd(benpy)** showing (**a**) the evolution of a single Bragg peak (011) versus temperature (250–175–250 K) and (**b**) the temperature dependence of the unit cell volume extracted from Le Bail analysis of the individual PXRD patterns.

3.3.2. Variable-Temperature Raman Spectroscopy

VT-Raman spectra were collected (150–2300 cm^{-1}; 250–150 K) to monitor vibrational transitions that occur with spin-state change. Figure 4a and Figure S12 show representative HS and LS patterns for **Pd(benpy)** and **Pt(benpy)**, respectively. The largest frequency shifts between spin states were the bands corresponding to the Fe–N and C≡N stretching, in agreement with the literature on Hofmann frameworks [44]. The characteristic Fe–N stretching peaks (<250 cm^{-1}) and C≡N bands (~2200 cm^{-1}) were upshifted from the HS to the LS state (Figure 4b and Figures S13 and S14). The C≡N bands also increased in intensity over the HS to LS transition (Figure 4b and Figure S14b, **Pd(benpy)** and **Pt(benpy)**, respectively).

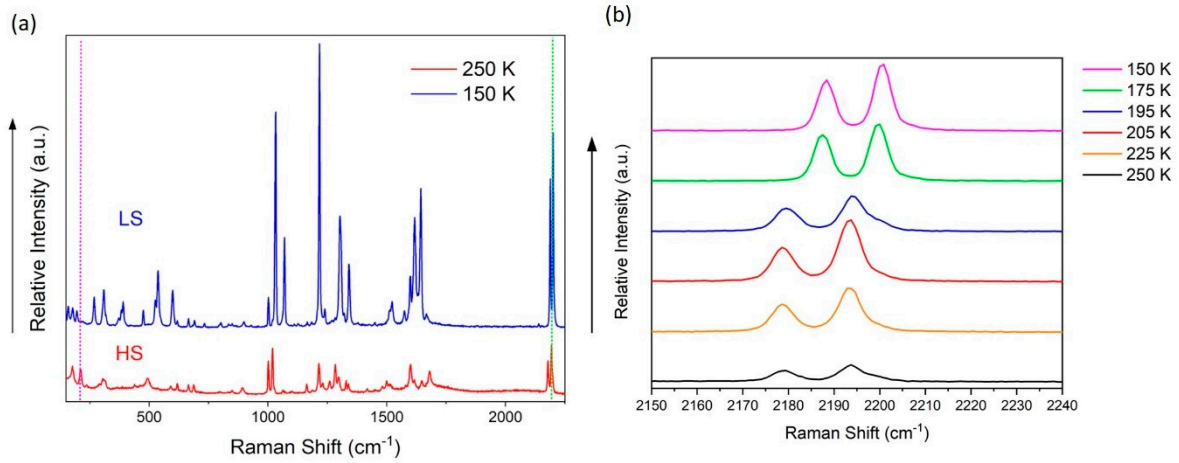

Figure 4. VT-Raman data for **Pd(benpy)** showing (**a**) representative HS (red) and LS (blue) spectra; the Fe–N and C≡N stretching regions are indicated by pink and green dotted lines, respectively. (**b**) The temperature dependence of the C≡N vibration.

3.3.3. Variable-Temperature, Single-Crystal X-ray Diffraction

Overall Structural Description

Powder diffraction analyses at 250 K confirmed that **Pd(benpy)** crystallizes in the primitive monoclinic space group: $P2_1/n$ and **Pt(benpy)** in the monoclinic *C*-centered space group $C2/m$ (Figures S6 and S7). SCXRD data collected on each agreed with this symmetry and space group assignment (Table 1). The asymmetric unit (ASU; Figure S15) of **Pd(benpy)** contained one Fe^{II} site, a half of a $[Pd(CN)_4)]^{2-}$ group, one benpy ligand, and one water molecule. The ASU (Figure S16) of **Pt(benpy)** contained one Fe^{II} site, a quarter of a $[Pd(CN)_4)]^{2-}$ group, one benpy ligand, and one water molecule. The main distinction between the two is that the benpy ligands showed a long-range, ordered, torsional twist around the amide bond in **Pd(benpy)** (Figure 5a). In **Pt(benpy)**, the benzyl ring of the ligand showed two-fold disorder (Figure 5b). Hence, the same ligand torsional ligand was observed but with short-range order, thus accounting for the space group difference between the analogues. The water molecule in **Pt(benpy)** was also disordered over two positions across the mirror plane.

Aside from the difference in symmetry, the overall formula for both was $[Fe^{II}(benpy)_2M(CN)_4]\cdot 2H_2O$, where M = Pd or Pt, and the Hofmann framework structures were similar. For each, the Fe^{II} sites were arranged in a distorted octahedral environment with an overall $[FeN_6]$ coordination, with the equatorial sites occupied by $[M(CN)_4]^{2-}$ groups, bound via the N atoms, and the axial sites occupied by benpy ligands, coordinated via a pyridyl N atom. The bridging of each Fe^{II} site by four $[M(CN)_4]^{2-}$ units, which, in turn, acted as four coordinating linkages, resulted in the formation of a 2-D layered-grid structure of the type $[Fe^{II}(M(CN)_4)]$, as shown in Figure 6. The benpy ligands extended above and below the $[Fe^{II}(M(CN)_4)]$ layers (Figure 6b,c). Neighboring benpy ligands along the *a*-direction were oriented in the same direction (Figure S17a), i.e., within each ligand the oxygen and amide

groups pointed in opposite directions and were oriented in the same direction compared to adjacent ligands. The *trans*-benpy ligands, i.e., those coordinated to the same Fe^{II} site, were related by inversion symmetry and, thus, the amide functional groups were facing in opposite directions (Figure S17b). Additionally, the $[Fe^{II}(M(CN)_4)]$ layers undulated along the *ab*-plane, as illustrated in Figure 6c.

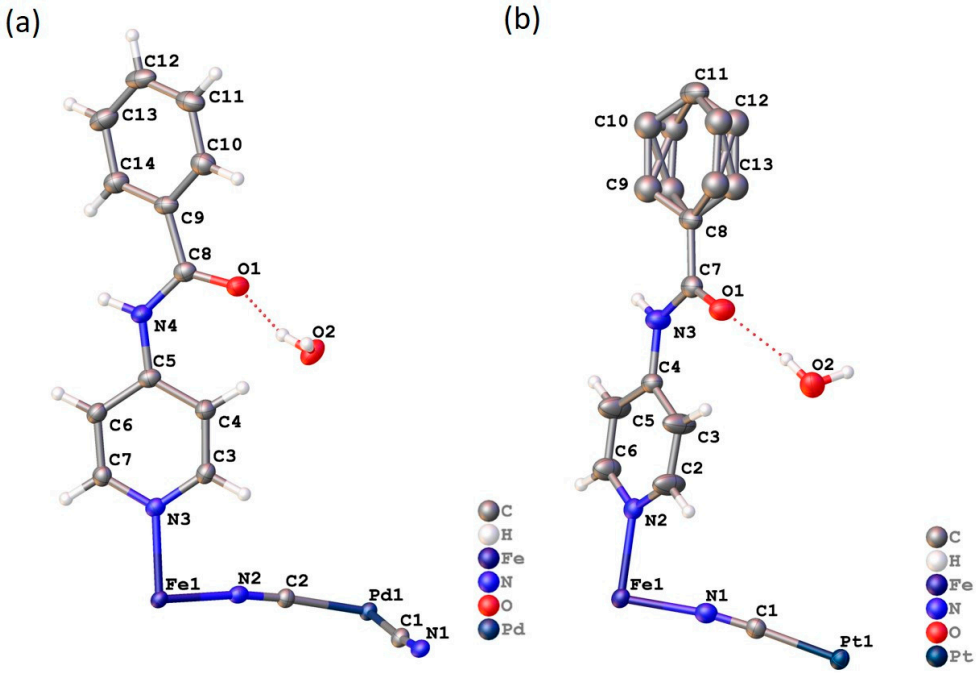

Figure 5. SCXRD thermal ellipsoid representation (50%) of the ASU of (**a**) **Pd(benpy)** and (**b**) **Pt(benpy)** at 100 K. Two-fold disorder in **Pt(benpy)** is shown.

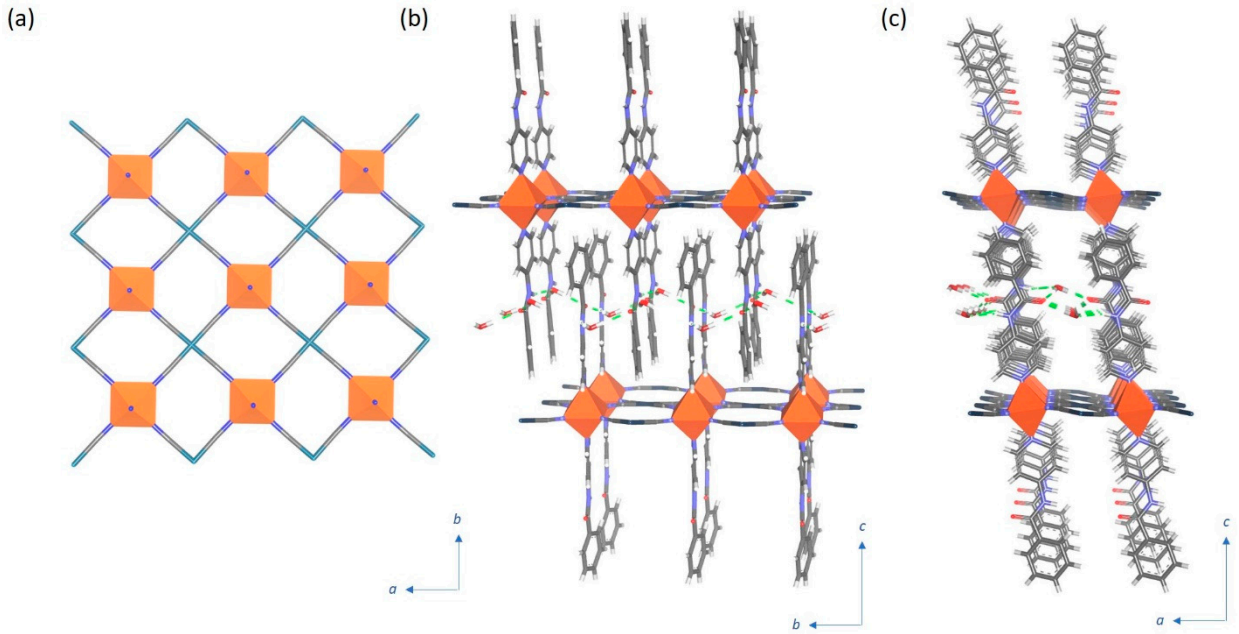

Figure 6. SCXRD structural representation of **Pd(benpy)** showing (**a**) the 2-D, grid-like Hofmann layers of the type $[Fe^{II}(Pd(CN)_4)]$, (**b**) the interdigitation of benpy ligands on adjacent 2-D layers, and (**c**) the head-to-tail overlap of interdigitated benpy ligand. The water molecules are located in the interlayer spacing and form hydrogen-bonding interactions with the benpy ligands (green).

Neighboring 2-D $[Fe^{II}(M(CN)_4)(benpy)_2]$ layers were stacked along the *c*-axis, with efficient packing provided by ligand interdigitation from neighboring layers (Figure 6b,c). The ligands of adjacent layers stacked in a head-to-tail fashion (Figure 6c) with near overlap. The nearly eclipsed overlap of the interdigitated ligands and close packing along the *b*-axis allowed for weak offset π-stacking, evidenced by the centroid-centroid distances between benpy ligands of ~3.5 Å (Figure 7). Two water molecules per Fe^{II} site were located in the interlayer spacing. These water molecules were engaged in a range of host–guest hydrogen-bonding interactions with the amide group of the benpy ligands (Figure 7). Similar arrays of host–guest interactions involving amide functional groups have been observed in other SCO frameworks [26–30].

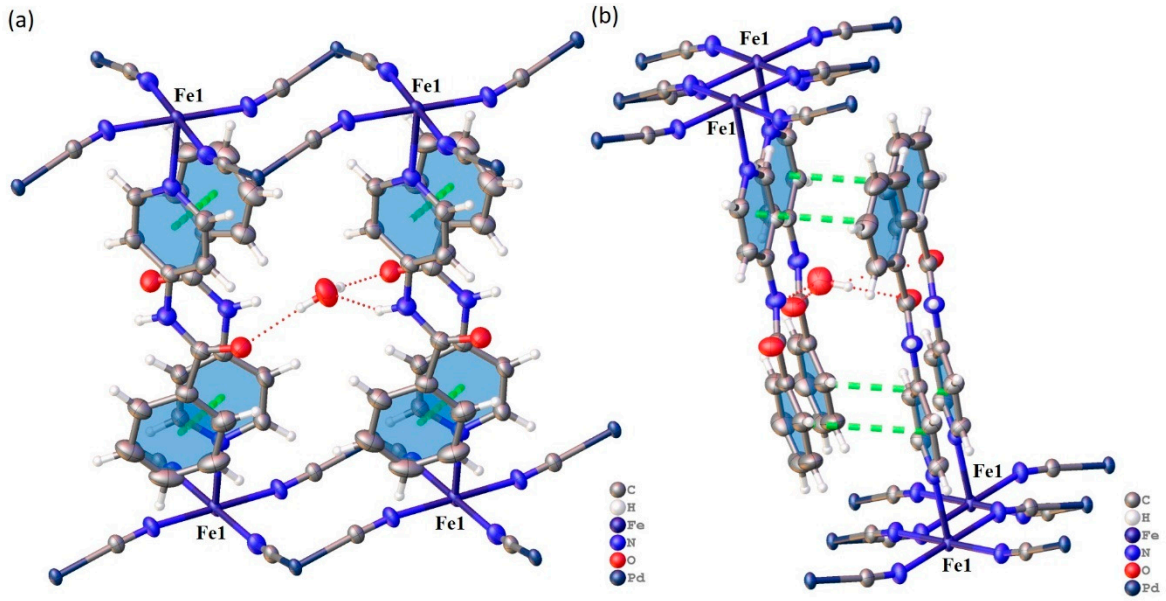

Figure 7. SCXRD structural representation of **Pd(benpy)** showing the position of the water molecules in the interlayer spacing, (**a**) the hydrogen-bonding interactions with the benpy ligands, and (**b**) the aromatic contacts.

Variable-Temperature Data

VT-SCXRD data were collected at 10-K intervals over the range of 250–100 K (HS to LS, cooling) for **Pd(benpy)** and 100–250 K (LS to HS, warming) for **Pt(benpy)**. Plots of the unit cell parameters (*a*-, *b*-, and *c*-axes) and unit cell volume versus temperature (Figures S18 and S19) matched the transition temperature anticipated from magnetic susceptibility. An overall 5.0% volume change was observed for both analogues over the HS to LS transition, consistent with a complete spin-state conversion. Notably, the evolution of the unit cell parameters was different for **Pd(benpy)** for **Pt(benpy)**. In particular, both the interlayer spacing (i.e., the *c*-axis) and the *β* angle increased over the HS to LS transition for **Pd(benpy)** but decreased for **Pt(benpy)**. The reason for this difference was not entirely clear but may have arisen from the relative structural support provided by the long- versus short-range order of the ligand torsion and water molecules for **Pd(benpy)** for **Pt(benpy)**, respectively.

Detailed structural analyses for **Pd(benpy)** for **Pt(benpy)** were conducted at 250 and 100 K to assess the structure changes over the HS to LS transition. Relevant parameters are summarized in Table S2. The overall variation to average Fe-N bond length for both was ~0.2 Å, which was consistent with a complete spin-state transition [10]. The octahedral distortion parameter (Σ), defined as the sum of the deviation from 90° of the 12 *cis*-N-Fe-N angles, is also a useful indicator of spin-state change. Typically, it is more regular in the LS state compared to the HS state [10]. However, for **Pd(benpy)** the degree of distortion was seen to increase over the HS to LS transition (HS = 8.16° and LS = 13.20°) and for **Pt(benpy)** there was no substantial change over the SCO transition. This is often an indicator of

elastic frustration [46–50], which arises from a competition between interactions and the volumetric change over the spin-state transition. In most cases, this results in multi-stepped SCO transitions, but here the cooperative one-step transition suggests that there was a degree of elastic frustration. However, it was not great enough to overcome the preferred energetics of the bulk material to attain spin-state homogeneity. Other minor changes to the structures included a contraction in host–guest hydrogen bonds and ligand–ligand aromatic contacts, as well as a more planar Hofmann layer in the LS state, as evidenced by change in Fe–N≡C angles toward 180°. Furthermore, the benpy torsional twist for both analogues decreased substantially with HS to LS transition. A notable distinction between **Pd(benpy)** and **Pt(benpy)** was that the guest-accessible void space was larger in **Pt(benpy)**, but for both analogues the void volume decreased with HS to LS transition (**Pd(benpy)**: 5% (73 Å^3) to 3% (37 Å^3) and **Pt(benpy)**: 13% (195 Å^3) to 6% (94 Å^3)). This distinction may underlie the difference in long-range and short-range ordering of the ligand torsional twist in **Pd(benpy)** and **Pt(benpy)**. Indeed, on closer inspection, the ligand–water contacts were slightly longer in **Pt(benpy)** compared to **Pd(benpy)** in the HS state (O1·water: 2.137(2) and 2.006(2) Å for Pt and Pd, respectively). These contacts may play a role in the ligand ordering.

4. Conclusions

Two isostructural 2-D Hofmann-like framework materials, $[Fe^{II}(benpy)_2M(CN)_4]\cdot 2H_2O$ (M = Pd, Pd), were prepared with a novel amide-functionalized ligand (benpy). Variation of M (Pd or Pt) resulted in subtle changes to structure and SCO properties, which we comprehensively assessed by variable temperature magnetic susceptibility, DSC, PXRD, Raman spectroscopy, and SCXRD analyses, and validated by calculation of the magnetic susceptibility data. The main change to the structure between the Pd and Pt analogues was the long- or short-range ordering of a torsional twist in the benpy ligand around the amide group. Structural analyses suggested this difference arose due to the relative steric bulk of Pd versus Pt and, hence, the packing efficiency and contacts that can be achieved. Both the Pd and Pt analogues showed abrupt and hysteretic one-step SCO transitions, with the Pt transition occurring at a slightly higher temperature. This difference was ascribed to a subtle variation HS stability arising from a combination of the greater electron density and size of Pt compared to Pd. Comparison of the HS and LS structures for both analogues revealed a degree of elastic frustration due to the increase in distortion over the HS to LS transition, opposed to the normal decrease, in particular, for the Pd analogue. Although, rather than a multi-step SCO transition, which can arise in such cases, a cooperative one-step character prevailed, indicating that the frustration effects were not large enough to overcome the preferential energetics of spin-state homogeneity. Consistent with this theory, we found that the net interactions were ferroelastic and that the transition was strongly cooperative. Overall, the inclusion of an amide-functionalized ligand into these SCO Hofmann frameworks successfully led to a range of through-bond (i.e., coordination bridges) and through-space (i.e., supramolecular contacts) pathways. Rather than functioning antagonistically, these functioned collectively to produce cooperative spin-state switching properties. This study supports the role of various structural modes of elastic coupling propagation in SCO materials.

Supplementary Materials: Additional synthetics, structural, and characterization data are available online at https://www.mdpi.com/2624-8549/3/1/26/s1.

Author Contributions: Conceptualization, M.A. and S.M.N.; investigation, X.O., M.A., L.X., A.T.B., C.H., K.A.Z. and Z.X.; calculations, B.J.P.; writing, X.O., C.J.K., B.J.P. and S.M.N. All authors have read and agreed to the published version of the manuscript.

Funding: This research was funded by The Australian Research Council (ARC; DP200100305).

Informed Consent Statement: Not applicable.

Data Availability Statement: Crystallographic data are freely available at the Cambridge Crystallographic Data Centre under 2049372-2049375.

Acknowledgments: We thank the ARC for Fellowships and Discovery Project funding. Access and use of the facilities of the Australian Synchrotron was supported by ANSTO. This research was facilitated by access to Sydney Analytical, a core research facility at the University of Sydney.

Conflicts of Interest: The authors declare no conflict of interest.

References

1. Kahn, O.; Kröber, J.; Jay, C. Spin Transition Molecular Materials for displays and data recording. *Adv. Mater.* **1992**, *4*, 718–728. [CrossRef]
2. Létard, J.-F.; Guionneau, P.; Goux-Capes, L. Towards Spin Crossover Applications. *Top. Curr. Chem.* **2004**, *235*, 221–249.
3. Gütlich, P.; Goodwin, H.A. Spin Crossover—An Overall Perspective. *Top. Curr. Chem.* **2004**, *233*, 1–47.
4. Gütlich, P.; Gaspar, A.B.; Garcia, Y. Spin state switching in iron coordination compounds. *Beilstein J. Org. Chem.* **2013**, *9*, 342–391. [CrossRef]
5. Halcrow, M.A. *Spin-Crossover Materials: Properties and Applications*; John Wiley & Sons: London, UK, 2013.
6. Kumar, K.S.; Ruben, M. Emerging trends in spin crossover (SCO) based functional materials and devices. *Coord. Chem. Rev.* **2017**, *346*, 176–205. [CrossRef]
7. Gütlich, P.; Hauser, A.; Spiering, H. Thermal and optical switching of Iron(II) Complexes. *Angew. Chem. Int. Ed.* **1994**, *33*, 2024. [CrossRef]
8. Real, J.A.; Gaspar, A.B.; Niel, V.; Muñoz, M.C. Communication between iron(II) building blocks in cooperative spin transi-tion phenomena. *Coord. Chem. Rev.* **2003**, *236*, 121–141. [CrossRef]
9. Real, J.A.; Gaspar, A.B.; Muñoz, M.C. Thermal, pressure and light switchable spin-crossover materials. *Dalton Trans.* **2005**, 2062–2079. [CrossRef]
10. Collet, E.; Guionneau, P. Structural analysis of spin-crossover materials: From molecules to materials. *C. R. Chim.* **2018**, *21*, 1133–1151. [CrossRef]
11. Spiering, H. Elastic Interaction in Spin-Crossover Compounds. *Top. Curr. Chem.* **2006**, 171–195. [CrossRef]
12. Nishino, M.; Boukheddaden, K.; Konishi, Y.; Miyashita, S. Simple Two-Dimensional Model for the Elastic Origin of Coopera-tivity among Spin States of Spin-Crossover Complexes. *Phys. Rev. Lett.* **2007**, *98*, 247203. [CrossRef]
13. Nishino, M.; Boukheddaden, K.; Miyashita, S. Molecular dynamics study of thermal expansion and compression in spin-crossover solids using a microscopic model of elastic interactions. *Phys. Rev. B* **2009**, *79*, 012409. [CrossRef]
14. Kitazawa, T.; Gomi, Y.; Takahashi, M.; Takeda, M.; Enomoto, M.; Miyazaki, A. Spin-crossover behaviour of the coordination polymer FeII(C5H5N)2NiII(CN)4. *J. Mater. Chem.* **1996**, *6*, 119. [CrossRef]
15. Niel, V.; Martinez-Agudo, J.M.; Munoz, M.C.; Gaspar, A.B.; Real, J.A. Cooperative spin crossover behavior in cya-nide-bridged Fe(II)−M(II) bimetallic 3D Hofmann-like networks (M= Ni, Pd, and Pt). *Inorg. Chem.* **2001**, *40*, 3838–3839. [CrossRef]
16. Muñoz, M.C.; Real, J.A. Thermo-, piezo-, photo- and chemo-switchable spin crossover iron(II)-metallocyanate based coordination polymers. *Coord. Chem. Rev.* **2011**, *255*, 2068–2093. [CrossRef]
17. Ni, Z.-P.; Liu, J.-L.; Hoque, N.; Liu, W.; Li, J.-Y.; Chen, Y.-C.; Tong, M.-L. Recent advances in guest effects on spin-crossover behavior in Hofmann-type metal-organic frameworks. *Coord. Chem. Rev.* **2017**, *335*, 28–43. [CrossRef]
18. Ohtani, R.; Hayami, S. Guest-Dependent Spin-Transition Behavior of Porous Coordination Polymers. *Chem. Eur. J.* **2017**, *23*, 2236–2248. [CrossRef] [PubMed]
19. Ohba, M.; Yoneda, K.; Agustí, G.; Muñoz, M.C.; Gaspar, A.B.; Real, J.A.; Yamasaki, M.; Ando, H.; Nakao, Y.; Sakaki, S.; et al. Bidirectional Chemo-Switching of Spin State in a Microporous Framework. *Angew. Chem. Int. Ed.* **2009**, *48*, 4767–4771. [CrossRef] [PubMed]
20. Southon, P.D.; Liu, L.; Fellows, E.A.; Price, D.J.; Halder, G.J.; Chapman, K.W.; Moubaraki, B.; Murray, K.S.; Létard, J.-F.; Kepert, C.J. Dynamic Interplay between Spin-Crossover and Host−Guest Function in a Nanoporous Metal−Organic Framework Material. *J. Am. Chem. Soc.* **2009**, *131*, 10998–11009. [CrossRef] [PubMed]
21. Klein, Y.M.; Sciortino, N.F.; Ragon, F.; Housecroft, C.E.; Kepert, C.J.; Neville, S.M. Spin crossover intermediate plateau stabilization in a flexible 2-D Hofmann-type coordination polymer. *Chem. Commun.* **2014**, *50*, 3838–3840. [CrossRef]
22. Liu, W.; Peng, Y.-Y.; Wu, S.-G.; Chen, Y.-C.; Hoque, N.; Ni, Z.-P.; Chen, X.-M.; Tong, M. Guest-Switchable Multi-Step Spin Transitions in an Amine-Functionalized Metal-Organic Framework. *Angew. Chem. Int. Ed.* **2017**, *56*, 14982–14986. [CrossRef]
23. Seredyuk, M.; Gaspar, A.B.; Ksenofontov, V.; Verdaguer, M.; Villain, F.; Gütlich, P. Thermal- and Light-Induced Spin Crossover in Novel 2D Fe(II) Metalorganic Frameworks {Fe(4-PhPy)2[MII(CN)x]y}·sH2O: Spectroscopic, Structural, and Mag-netic Study. *Inorg. Chem.* **2009**, *48*, 6130–6141. [CrossRef] [PubMed]
24. Liu, W.; Wang, L.; Su, Y.-J.; Chen, Y.-C.; Tucek, J.; Zboril, R.; Ni, Z.-P.; Tong, M.-L. Hysteretic Spin Crossover in Two-Dimensional (2D) Hofmann-Type Coordination Polymers. *Inorg. Chem.* **2015**, *54*, 8711–8716. [CrossRef] [PubMed]
25. Noveron, J.C.; Lah, M.S.; Del Sesto, R.E.; Arif, A.M.; Miller, J.S.; Stang, P.J. Engineering the Structure and Magnetic Properties of Crystalline Solids via the Metal-Directed Self-Assembly of a Versatile Molecular Building Unit. *J. Am. Chem. Soc.* **2002**, *124*, 6613–6625. [CrossRef] [PubMed]

26. Valverde-Muñoz, F.J.; Bartual-Murgui, C.; Piñeiro-López, L.; Muñoz, M.C.; Real, J.A. Influence of host-guest and host-host interactions on the spin-crossover of 3D Hofmann-type clathrates {FeII(pina)[MI(CN)2]2}·xMeOH (MI = Ag, Au). *Inorg. Chem.* **2019**, *58*, 10038–10046. [CrossRef]
27. Lan, W.; Valverde-Muñoz, F.J.; Dou, Y.; Hao, Y.; Muñoz, M.C.; Zhou, Z.; Liu, H.; Liu, Q.; Real, J.A.; Zhang, D. A thermal- and light-induced switchable one-dimensional rare loo-like spin crossover coordination polymer. *Dalton Trans.* **2019**, *48*, 17014. [CrossRef]
28. Hao, X.; Dou, T.; Cao, L.; Yang, L.; Liu, H.; Li, D.; Zhang, D.; Zhou, Z. Tuning of crystallization method and ligand confor-mation to give a mononuclear compound or two-dimensional SCO coordination polymer based on a new semi-rigid V-shaped bis-pyridyl bis-amide ligand. *Acta Cryst.* **2020**, *C76*, 412–418.
29. Mondal, D.J.; Roy, S.; Yadav, J.; Zeller, M.; Konar, S. Solvent-induced reversible spin-crossover in a 3D Hofmann-type coor-dination polymer and unusual enhancement of the lattice cooperativity at the desolvated state. *Inorg. Chem.* **2020**, *59*, 13024–13028. [CrossRef] [PubMed]
30. Ahmed, M.; Xie, Z.; Thoonen, S.; Hua, C.; Kepert, C.J.; Price, J.R.; Neville, S.M. A new spin crossover FeII coordination environment in a two-fold interpenetrated 3-D Hofmann-type framework material. *Chem. Commun.* **2021**, *57*, 85–88. [CrossRef]
31. Cowieson, N.P.; Arago, D.; Clift, M.; Ericsson, D.J.; Gee, C.; Harrop, S.J.; Mudie, N.; Panjikar, S.; Price, J.R.; Ribol-di-Tunnicliffe, A.; et al. MX1: A bending-magnet crystallography beamline serving both chemical and macromolecular crystallographic communities at the Australian Synchrotron. *J. Synch. Rad.* **2015**, *22*, 187–190. [CrossRef]
32. McPhillips, T.M.; McPhillips, S.E.; Chiu, H.-J.; Cohen, A.E.; Deacon, A.M.; Ellis, P.J.; Garman, E.; Gonzalez, A.; Sauter, N.K.; Phiza-ckerley, R.P. Blu-Ice and the Distributed Control System: Software for data acqui-sition and instrument control at macromolecular crystallography beamlines. *J. Synch. Rad.* **2002**, *9*, 401–406. [CrossRef] [PubMed]
33. Kabsch, W. XDS. *Acta Cryst. D* **2010**, *66*, 125–132. [CrossRef]
34. Sheldrick, G.M. SHELXT–Integrated space-group and crystal-structure determination. *Acta Cryst. Sect. A* **2015**, *71*, 3–8. [CrossRef] [PubMed]
35. Sheldrick, G.M. Crystal structure refinement with SHELXL. *Acta Cryst. Sect. C* **2015**, *71*, 3–8. [CrossRef] [PubMed]
36. Dolomanov, O.V.; Bourhis, L.J.; Gildea, R.J.; Howard, J.A.K.; Puschmann, H. OLEX2: A complete structure solution, refinement and analysis program. *J. Appl. Crystallogr.* **2009**, *42*, 339–341. [CrossRef]
37. Wallwork, K.S.; Kennedy, B.J.; Wang, D.C. The High Resolution Powder Diffraction Beamline for the Australian Synchrotron. In *Fourth Huntsville Gamma-Ray Burst Symposium*; AIP Publishing: New York, NY, USA, 2007; Volume 879, pp. 879–882.
38. Bergamaschi, A.; Cervellino, A.; DiNapoli, R.; Gozzo, F.; Henrich, B.; Johnson, I.; Kraft, P.; Mozzanica, A.; Schmitt, B.; Shi, X. The MYTHEN detector for X-ray powder diffraction experiments at the Swiss Light Source. *J. Synchrotron Radiat.* **2010**, *17*, 653–668. [CrossRef] [PubMed]
39. Jong, L.; Ruben, G.; Spear, K. *PDViPeR*; Synchrotron Light Source Australia Pty Ltd.: Melbourne, Australia, 2014.
40. Coelho, A. *TOPAS Version 4.1*; Bruker AXS GmbH: Karlsruhe, Germany, 2007.
41. Wajnflasz, J.; Pick, R. Transitions «Low spin»-«High spin» dans les complexes de $Fe2^{+}$. *J. Phys.* **1971**, *32*, 90–91. [CrossRef]
42. Pavlik, J.; Boča, R. Established Static Models of Spin Crossover. *Eur. J. Inorg. Chem.* **2013**, *5–6*, 697–709. [CrossRef]
43. Ruzzi, G.; Cruddas, J.; McKenzie, R.H.; Powell, B.J. Equivalence of elastic and Ising models for spin crossover materials. *arXiv* **2020**, arXiv:2008.08738.
44. Ragon, F.; Yaksi, K.; Sciortino, N.F.; Chastanet, G.; Létard, J.-F.; D'Alessandro, D.M.; Kepert, C.J.; Neville, S.M. Thermal Spin Crossover Behaviour of Two-Dimensional Hofmann-Type Coordination Polymers Incorporating Photoactive Ligands. *Aust. J. Chem.* **2014**, *67*, 1563–1573. [CrossRef]
45. Roubeau, O.; Castro, M.; Burriel, R.; Haasnoot, J.G.; Reedijk, J. Calorimetric Investigation of Triazole-Bridged Fe(II) Spin-Crossover One-Dimensional Materials: Measuring the Cooperativity. *J. Phys. Chem. B* **2011**, *115*, 3003–3012. [CrossRef] [PubMed]
46. Molnár, G.; Mikolasek, M.; Ridier, K.; Fahs, A.; Nicolazzi, W.; Bousseksou, A. Molecular Spin Crossover Materials: Review of the Lattice Dynamical Properties. *Annalen Physik* **2019**, *531*, 1900076. [CrossRef]
47. Kulmaczewski, R.; Olguín, J.; Kitchen, J.A.; Feltham, H.L.C.; Jameson, G.N.L.; Tallon, J.L.; Brooker, S. Remarkable Scan Rate Dependence for a Highly Constrained Dinuclear Iron(II) Spin Crossover Complex with a Wide Thermal Hysteresis Loop. *J. Am. Chem. Soc.* **2014**, *136*, 878–881. [CrossRef] [PubMed]
48. Paez-Espejo, M.; Sy, M.; Boukheddaden, K. Elastic Frustration Causing Two-Step and Multistep Transitions in Spin-Crossover Solids: Emergence of Complex Antiferroelastic Structures. *J. Am. Chem. Soc.* **2016**, *138*, 3202–3210. [CrossRef]
49. Cruddas, J.; Powell, B.J. Structure-property relationships and the mechanism of multistep transitions in spin crossover mate-rials and frameworks. *Inorg. Chem. Front.* **2020**, *7*, 4424–4437. [CrossRef]
50. Cruddas, J.; Powell, B.J. Spin-State Ice in Elastically Frustrated Spin-Crossover Materials. *J. Am. Chem. Soc.* **2019**, *141*, 19790–19799. [CrossRef] [PubMed]